Bioactive Materials 6 (2021) 3865–3878

Contents lists available at ScienceDirect

Bioactive Materials

journal homepage: www.sciencedirect.com/journal/bioactive-materials

Leukocyte/platelet hybrid membrane-camouflaged dendritic large pore mesoporous silica nanoparticles co-loaded with photo/chemotherapeutic agents for triple negative breast cancer combination treatment

Tao Zhang [a,1], Hui Liu [a,1], Ling Li [a,1], Zhaoyang Guo [a], Jia Song [a], Xiaoying Yang [a], Guoyun Wan [b], Rongshan Li [a,*], Yinsong Wang [a,**]

[a] Tianjin Key Laboratory on Technologies Enabling Development of Clinical Therapeutics and Diagnostics (Theranostics), The Province and Ministry Co-Sponsored Collaborative Innovation Center for Medical Epigenetics, Department of Pharmaceutics, School of Pharmacy, Tianjin Medical University, Tianjin, 300070, China
[b] The Key Laboratory of Biomedical Material, School of Life Science and Technology, Xinxiang Medical University, Xinxiang, 453003, China

ARTICLE INFO

Keywords:
Leukocyte/platelet hybrid membrane
Dendritic large pore mesoporous silica nanoparticles
Triple-negative breast cancer
Phototherapy
Chemotherapy

ABSTRACT

Triple-negative breast cancer (TNBC) is an aggressive subset of breast cancer and currently lacks effective therapeutic targets. As two main phototherapeutic methods, photothermal therapy (PTT) and photodynamic therapy (PDT) show many advantages in TNBC treatment, and their combination with chemotherapy can achieve synergistic therapeutic effects. In the present study, a biomimetic nanoplatform was developed based on leukocyte/platelet hybrid membrane (LPHM) and dendritic large pore mesoporous silicon nanoparticles (DLMSNs). A near infrared (NIR) fluorescent dye IR780 and a chemotherapeutic drug doxorubicin (DOX) were co-loaded into the large pores of DLMSNs to prepare DLMSN@DOX/IR780 (DDI) nanoparticles (NPs), followed by camouflage with LPHM to obtain LPHM@DDI NPs. Through the mediation of LPHM, LPHM@DDI NPs showed an excellent TNBC-targeting ability and very high PTT/PDT performances *in vitro* and *in vivo*. Upon NIR laser irradiation, LPHM@DDI NPs exhibited synergistic cytotoxicity and apoptosis-inducing activity in TNBC cells, and effectively suppressed tumor growth and recurrence in TNBC mice through tumor ablation and anti-angiogenesis. These synergistic effects were sourced from the combination of PTT/PDT and chemotherapy. Altogether, this study offers a promising biomimetic nanoplatform for efficient co-loading and targeted delivery of photo/chemotherapeutic agents for TNBC combination treatment.

1. Introduction

Triple-negative breast cancer (TNBC) is an aggressive subset of breast cancer and characterized clinically by the lack of estrogen and progesterone receptor expressions and the absence of overexpression of human epidermal growth factor 2 receptor. Because there are no effective therapeutic targets, TNBC has been a difficult problem in clinic [1,2]. Chemotherapy is one of the major methods for TNBC treatment, but toxic side effects of chemotherapeutic agents due to lacking tumor selectivity and drug resistance occurring after long term use often lead to the failure of TNBC chemotherapy [3]. Although immunotherapy brings hope to TNBC patients, it is not always effective. For instance, blocking the programmed death 1/programmed death ligand 1 interaction has been proved to be effective for only approximately 20% of TNBC [4,5]. Hence, exploring efficient therapeutic strategies is becoming extremely urgent for TNBC treatment.

Phototherapy is a topical remedy that shows many advantages such as non or minimal invasion, time and space controllability, and less susceptibility to drug resistance for cancer treatment [6,7]. As two main phototherapeutic methods, photothermal therapy (PTT) and photodynamic therapy (PDT) have been widely applied in the field of cancer research. PTT agents can convert light energy to thermal energy to ablate solid tumors directly through heating effect. PDT is carried out by using photosensitizers and molecular oxygen under the laser irradiation

Peer review under responsibility of KeAi Communications Co., Ltd.
* Corresponding author.
** Corresponding author.
E-mail addresses: lirongshan@tmu.edu.cn (R. Li), wangyinsong@tmu.edu.cn (Y. Wang).
[1] T. Zhang, H. Liu and L. Li contributed equally to this work.

https://doi.org/10.1016/j.bioactmat.2021.04.004
Received 2 September 2020; Received in revised form 27 March 2021; Accepted 1 April 2021

at particular wavelength to produce reactive oxygen species (ROS) that have strong toxicity to tumor cells. In addition, PTT and PDT can also suppress tumor angiogenesis and activate antitumor immunity to inhibit tumor growth and metastasis indirectly [8–10]. Some near-infrared (NIR) fluorescent dyes possess PTT/PDT efficiencies upon laser irradiation and can realize double therapy simultaneously [11–13]. As one of these NIR fluorescent dyes, IR780 has been regarded as a promising phototherapeutic agent owing to its PTT/PDT performances. In our previous investigations, IR780 was used as a phototherapeutic agent to combine with chemotherapy and displayed synergistic anticancer effects [14,15]. However, phototherapeutic and chemotherapeutic agents have different pharmacokinetic behaviors, so it is difficult to ensure their consistent *in vivo* processes and specific tumor-accumulations. Therefore, developing an efficient carrier system for their co-loading and targeting delivery has been considered as an optimal strategy for cancer combination treatment [16].

As a novel drug carrier platform, mesoporous silica nanoparticles (MSNs) have good biological properties e.g., biocompatibility, biodegradability and nontoxicity as well as some unique structural characteristics including tailored mesoporous channels, uniform pore size distribution and high surface area [17,18]. However, because of narrow channels and small pore openings, traditional MSNs are not suitable for carrying macromolecule drugs or co-loading multiple different drugs. By comparison, dendritic large pore mesoporous silica nanospheres (DLMSNs) have greatly increased pore size and porosity, and consequently show an elevated drug-loading capacity [19–21]. Hence, DLMSNs are regarded to be more suitable for co-loading phototherapeutic and chemotherapeutic agents for TNBC combination treatment. In our recent study [22], we have successfully prepared DLMSNs with desired channel morphologies and pore sizes using the dual-templating method with different auxiliary templates for loading selective drugs. However, some disadvantages are accompanied by the structural features of DLMSNs, e.g., the large internal channels make the loaded drugs easily to leak from DLMSNs during their *in vivo* delivery and the high surface area increases the chance of DLMSNs to be eliminated by the immune system owing to the protein absorption in blood circulation. It thus can be seen that surface modification of DLMSNs with appropriate materials is very important for blocking their opening pores, prolonging their circulation time, and even delivering them targetedly [23,24].

In recent years, biomimetic camouflage of nanoparticles (NPs) with cell membranes isolated from red blood cells, platelet, stem cells, immune cells, and cancer cells has been of great concern [25,26]. Many investigations have used various cell membranes as a novel kind of pore-blocking agents to camouflage MSNs, thus given them superior biological properties such as enhanced *in vivo* stability, prolonged circulation time, self-recognition and homotypic targeting capability [27–29]. In addition, the camouflage with hybrid membrane derived from different cells can endow NPs flexibility and controllable functions [30,31]. Leukocytes play important roles in protection against microorganism infection, cancer cells and parasites. Generally, leukocytes reach their action targets through cellular membrane interactions to exert their functions. Integrin lymphocyte function-associated antigen-1 (LFA-1) is a surface membrane molecule expressed on leukocytes and its specific ligand intercellular adhesion molecule-1 (ICAM-1) is often highly expressed in tumor-associated vasculature [32]. A recent investigation has shown that leukocyte membrane-coated NPs can efficiently activate the LFA-1/ICAM-1 adhesion pathway and thus increase tumor vascular permeability through VE-cadherin phosphorylation, resulting in enhanced penetration of NPs through tumor blood vessels [33]. It is well known that P-selectin expressed on platelet membrane can interact with P-selectin glycoprotein ligand-1 on leukocyte membrane and thus mediate leukocytes rolling on endothelial membrane [34]. This indicates that hybrid membrane can be easily prepared from platelet and leukocyte membranes through their specific interaction. P-selectin is also a ligand for CD44 receptor, which has been verified to be overexpressed on TNBC cells [35]. Therefore, we believe that DLMSNs camouflaged with lymphocyte/platelet hybrid membrane (LPHM) may be of dual-targeting ability for TNBC therapy, including LFA-1/ICAM-1 interaction-dependent tumor vascular targeting and penetration ability and P-selectin/CD44 binding-mediated tumor cell targeting ability.

In this study, we designed a biomimetic nanoplatform through camouflaging DLMSNs with LPHM for efficient co-loading and selective co-delivery of IR780 and DOX, in an attempt to obtain synergistic effects of PTT/PDT combined with chemotherapy against TNBC. As shown in Fig. 1A, IR780 and DOX are co-loaded inside the large pores of DLMSNs through physical adsorption to prepare DLMSN@DOX/IR780 (DDI) NPs. LPHM is prepared using a simple and quick method as previously reported [30] and then absorbed onto DDI NPs by sonication to acquire LPHM@DDI NPs. Fig. 1B illustrates the *in vivo* action mechanisms of LPHM@DDI NPs against TNBC. After intravenous injection, LPHM@DDI NPs can arrive and further be accumulated in TNBC tumor via LFA-1/ICAM-1 interaction-dependent tumor vascular targeting and crossing effects, and next be uptaken by TNBC cells specifically through the mediation of P-selectin/CD44 specific binding. Upon NIR laser irradiation, IR780 in LPHM@DDI NPs exerts PTT/PDT efficacies to ablate TNBC tumor and destroy tumor microenvironment by rising the local temperature of tumor and promoting the production of ROS. PTT/PDT performances can also accelerate the release of DOX from LPHM@DDI NPs to exert suppression effects on TNBC recurrence.

2. Materials and methods

2.1. Materials

IR-780, 2′,7′-dichloro-dihydrofluorescein diacetate (DCFH-DA) and cetyl trimethyl ammonium bromide (CTAB) were purchased from Sigma-Aldrich (St Louis, MO, USA). DOX, 4′,6′-diamidine-2′-phenylindole (DAPI) and singlet oxygen sensor green (SOSG) were bought from Meilun Biotech (Dalian, China). Sodium salicylate (NaSal) and tetraethyl orthosilicate (TEOS) were purchased from Heowns Biochemical Technology (Tianjin, China). Annexin-V-FITC/7AAD apoptosis kit was bought from (BD Biosciences, San Jose, USA). LIVE/DEAD cell imaging kit and monoclonal antibodies against CD11a-FITC and CD62P-APC were provided by eBioscience (San Diego, CA, USA). Coomassie brilliant blue methylthiazolyldiphenyl-tetrazolium bromide (MTT) and TUNEL apoptosis assay kit were sourced from SolarbioScience & Technology (Beijing, China). Rabbit anti-CD31 polyclonal antibody was purchased from Abcam (Cambridge, MA, USA).

2.2. Cell lines and animals

Mouse TNBC cell line 4T1 and mouse macrophage cell line Raw 264.7 were sourced from BioVector NTCC (Beijing, China). These cells were cultured in DMEM (L120KJ, Gibco, Life Technologies) with adding of 10% fetal bovine serum (FBS) and 1% penicillin/streptomycin in an incubator under an atmosphere of 95% air and 5% CO_2 at 37 °C. For laser irradiation, the cells were irradiated with an 808 nm laser for 2 min after incubation with therapeutic agents for 2 h and the irradiation intensity was 2 W/cm^2. All the cell experiments were described detailedly in the section of Supporting Information.

BALB/c mice (female, six to eight weeks old) were provided by SPF Biotechnology Co., Ltd. (Beijing, China). 5.0×10^5 of 4T1 cells were inoculated into the mouse groin through subcutaneous injection to construct TNBC animal model. For combination treatment, the mice bearing 4T1 tumors were intravenously injected with antitumor agents and 12 h later received the 808 nm laser irradiation with an intensity of 2 W/cm^2 at tumor site for 10 min. The animal experiments in this study were performed in accordance with the guidelines that have been approved by the Animal Ethics Committee of Tianjin Medical University and fully described in the section of Supporting Information.

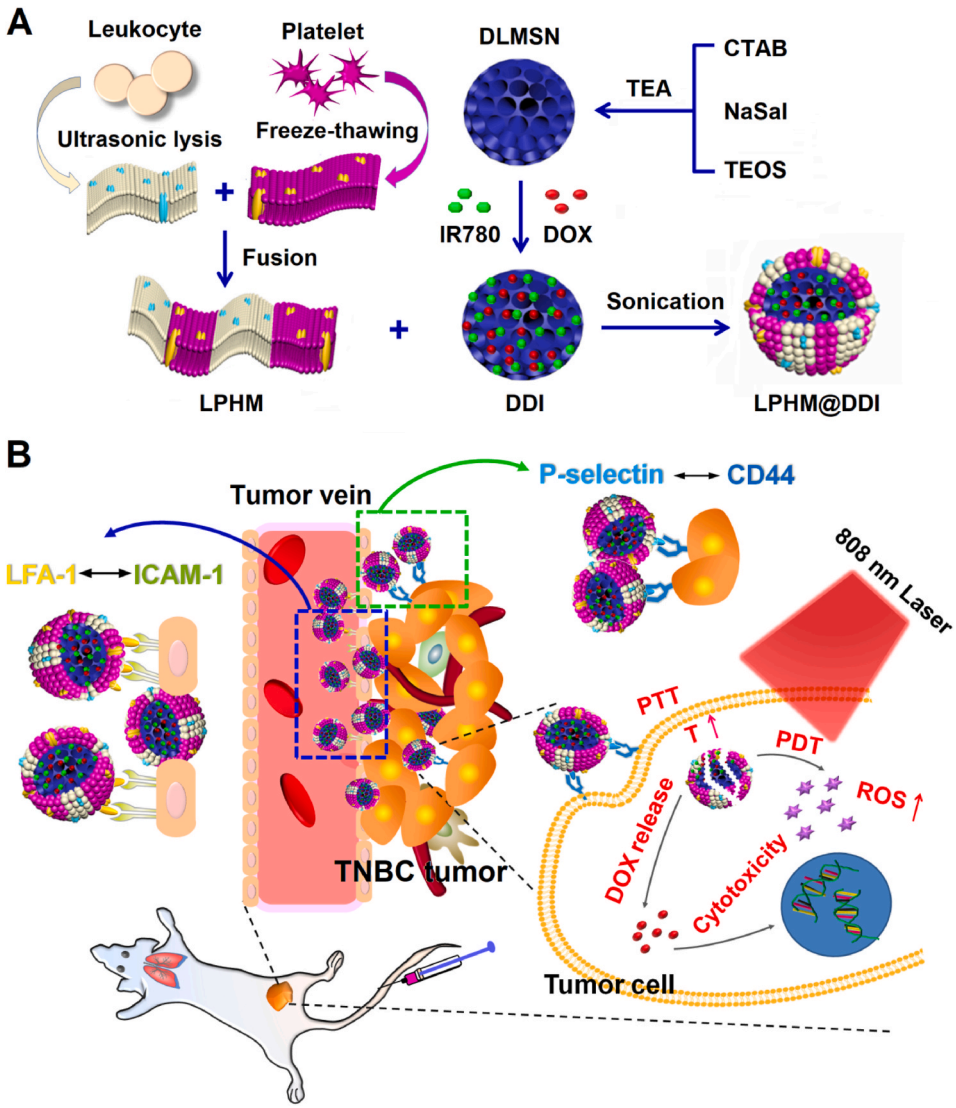

Fig. 1. Schematic illustrations for preparation method of LPHM@DDI NPs (A) and their synergistic effects in TNBC treatment via combining PTT/PDT with chemotherapy (B).

2.3. Preparation and characterization of DLMSNs and DDI NPs

DLMSNs were prepared using a dual-template sol-gel method as we previously reported [22]. 0.3 g of CTAB and 0.05 g of NaSal were soluble in 20 mL of deionized water with adding of 0.25% of triethyl amine (TEA) and stirred for 3 h at 80 °C. Next, 3.2 mL of TEOS was added dropwise and further stirred for 2 h, thus ensuring complete hydrolysis-polycondensation of TEOS. The obtained DLMSNs were collected by 20-min centrifugation at 15,000 rpm and washed with methanol several times. To remove CTAB, approximately 100 mg of DLMSNs were dispersed in 40 mL of methanol containing 3.5% hydrochloric acid under stirring for 24 h at 70 °C. After centrifugation and washing, DLMSNs were vacuum dried for the following use.

DOX and IR780 were co-loaded into DLMSNs through simple adsorption process to prepare DDI NPs. 10 mg of DLMSNs were first dispersed in 1 mL of methanol. 4 mg of DOX and 2 mg of IR780 were dissolved in 1 mL of methanol and next mixed with DLMSNs under continuous stirring for 3 d at room temperature. The mixture was centrifuged at 15,000 rpm and washed with methanol to obtain DDI NPs. Meanwhile, the supernatant was collected for further detecting the loading contents of DOX and IR780 in DDI NPs with an UV-2450 ultraviolet–visible–near infrared (UV–Vis–NIR) spectrophotometer (Shimadzu, Kyoto, Japan) at 480 nm and 780 nm, respectively.

DLMSNs and DDI NPs were observed morphologically under a transmission electron microscope (TEM) (Hitachi HT7700, Tokyo, Japan). Their particle diameters, polydispersity indexes (PDIs) and zeta potentials were measured with an instrument of zeta-sizer (Nano ZS-90, Malvern, UK). The surface area and pore size of DLMSNs were obtained from the nitrogen adsorption-desorption isotherm determined using an ASAP2020 specific surface area and aperture analyzer (Micromeritics, Norcross, GA, USA). The distributions of Si, O, C, and N elements in DDI NPs were analyzed with a JEM-2100F instrument of energy-dispersive X-ray spectroscopy (EDS)-mapping (JEOL, Tokyo, Japan).

2.4. Preparation and characterization of LPHM@DDI NPs

Lymphocyte membrane (LM) debris was extracted from quantitative Raw 264.7 cells according to a traditional method [33]. Platelets were sourced from the normal mice and their membrane (PM) debris was extracted by using the repeated freeze-thawing method as previously reported [35]. For preparation of LPHM, LM derived from 1.25×10^6 Raw 264.7 cells and PM derived from 7.5×10^7 platelets were incubated in phosphate buffer saline (PBS, pH = 7.4, 1 mL) under stirring for 10 min at 37 °C. 1 mg of DDI NPs prepared above was added and followed

by sonication for 2 min to obtain LPHM@DDI NPs. LM@DDI and PM@DDI NPs were also prepared for comparison from 1 mg of DDI NPs mixed separately with LM derived from 5×10^6 Raw 264.7 cells and PM derived from 1.0×10^7 platelets. Blank DLMSNs camouflaged with different membrane debris including LM@DLMSNs, PM@DLMSNs and LPHM@DLMSNs were also prepared meantime.

LPHM@DDI NPs were observed morphologically under a TEM. Their particle diameter, PDI and Zeta potential were measured by an instrument of zeta-sizer. For evaluating the *in vitro* stability of LPHM@DDI NPs, the size and zeta potential changes of DMLMNs, DDI and LPHM@DDI NPs were further monitored while 5-day storage in deionized water as well as in 10% FBS at 4 °C. In addition, the spectral features and optical stabilities of DOX, IR780, DDI NPs, LPHM@DLMS NPs, and LPHM@DDI NPs during 5-day storage were also assessed by an UV–Vis–NIR spectrophotometer.

2.5. Surface protein characterization of LPHM@DDI NPs

First, the surface proteins on DLMSNs, LM, PM, LM@DLMSNs, PM@DLMSNs, and LPHM@DLMSNs were separated by sodium dodecyl sulfate-polyacrylamide gel electrophoresis and then processed with staining of Coomassie brilliant blue reagent. The protein components were characterized and imaged with a digital camera. Moreover, the protein levels of LFA-1 (CD11a) and P-selectin (CD62P) on LM@DLMSNs, PM@DLMSNs and LPHM@DLMSNs were processed with double staining of anti-mouse CD11a-FITC and anti-human/mouse CD62P-APC antibodies according to the manufacture's protocols and then assayed using an Accuri C6 flow cytometer (BD Biosciences, California, USA).

2.6. In vitro evaluation of drug release property

The DOX releases from DDI and LPHM@DDI NPs alone and their preprocessing with laser irradiation were evaluated *in vitro* at different pH values. 1 mL of sample solutions containing about 0.5 μg/mL DOX were put into the dialysis bags with a 12–14 kDa molecular mass cutoff and some of them were irradiated with an 808 nm laser at an intensity of 2 W/cm^2 for 10 min. After that, all sample solutions were dialyzed separately in 20 mL of PBS media with pH values of 5.5, 6.5 and 7.4 in a shaking incubator at 37 ± 0.2 °C with a shaking velocity of 100 rpm for 72 h. After dialysis for predetermined times, all the release media were collected and replaced with 20 mL of fresh release media. The concentrations of DOX in these collected release media were measured at 480 nm using an UV–Vis spectrophotometer. Accordingly, the DOX released amounts were further calculated.

2.7. In vitro evaluation of PTT/PDT performance

The PTT efficiencies of IR780, DDI NPs and LPHM@DDI NPs were determined by assessing their temperature elevation effects during a 10 min period of 808 nm laser irradiation with an intensity of 2 W/cm^2. Within the whole irradiation period, the thermal images of these PTT agents were recorded with an IR thermal imaging camera (FLIR Corporation, USA). In the meantime, DLMSNs and DOX were also determined for comparisons. The concentrations of DOX and IR780 in the above sample solutions were 37.5 and 50 μg/mL, respectively.

The PDT efficiencies of IR780, DDI NPs and LPHM@DDI NPs were assessed by determining the ROS generation levels using SOSG as a fluorescence probe after different times of laser irradiation. Briefly, the sample solutions containing SOSG were given the 808 nm laser irradiation at an intensity of 2 W/cm^2 for 2, 4, 6, 8, and 10 min separately. After that, the ROS-activated SOSG in these sample solutions were analyzed by a fluorescence spectrophotometer. DLMSNs and DOX were also determined for comparisons. Moreover, all these sample solutions containing SOSG but without receiving laser irradiation were also determined at the same time.

2.8. Statistical analysis

Statistical analysis was performed by using Student's test or one-way analysis of variance (ANOVA). $P < 0.05$ and $P < 0.01$ were respectively regarded as significant difference and very significant difference.

3. Results and discussion

3.1. Preparation and characterization of LPHM@DDI NPs

DLMSNs have been considered as an excellent carrier material for loading macromolecular drugs or co-loading multiple different drugs due to their small particle size and large internal pores. In our previous report [22], we successfully prepared DLMSNs with adjustable pore structures (pore morphology and pore size) using the dual-template method through applying different auxiliary templates and also discussed the formation mechanism of DLMSNs, thus provided a guiding principle for preparation of DLMSNs suitable for their biomedical applications. In this study, CTAB and NaSal were used as the major and auxiliary templates respectively to prepare DLMSNs with large pore size for efficient co-loading of IR780 and DOX. DLMSNs thus prepared exhibited a uniform spherical shape with very clear large pore structure (Fig. S1A) and an average particle size of approximately 141.1 ± 15.8 nm (Fig. S1B). Owing to the presence of surface silicon hydroxyl groups, DLMSNs showed a negative zeta potential of −20.5 ± 6.5 mV. The nitrogen adsorption-desorption isotherm and the pore size distribution of DLMSNs are shown in Fig. S1C and S1D. By using the Brunauer-Emmett-Teller equation, the surface area and pore volume of DLMSNs were calculated and their values were 861 m^2/g and 1.10 cm^3/g, respectively. In accordance with the density-functional theory, the calculated average pore diameter was 9.2 nm. Hence, it can be deduced that DLMSNs prepared in this study have a large drug loading capacity.

Next, IR780 and DOX were co-loaded inside the large pores of DLMSNs through simple physical adsorption to prepare DDI NPs. As shown in the TEM images (Fig. 2A), the internal channels of DLMSNs were obviously loaded with in DDI NPs. In the EDS-mapping images of DDI NPs (Fig. 2B), the elemental signal of Si came from DLMSNs and the elemental signals of C and N were sourced from DOX and IR780. These results demonstrated that these two therapeutic agents were efficiently loaded into DLMSNs. The loading contents of IR780 and DOX in DDI NPs measured using the UV–Vis–NIR spectrophotometric method were 10.0 ± 2.4% and 13.3 ± 1.2%, respectively. LM and PM were extracted separately from leukocytes and platelets and next fused to form hybrid membrane LPHM. After that, LPHM was wrapped onto the surfaces of DDI NPs through sonication process to obtain biomimetic LPHM@DDI NPs. As shown in Fig. 2A, LPHM existed on the surfaces of LPHM@DDI NPs clearly and blocked the pore openings successfully. DDI NPs showed an almost identical particle size (143.6 ± 12.5 nm) to that of DLMSNs (Fig. 2B), but in the meantime their zeta potential significantly changed to −5.03 ± 2.3 mV (Fig. 2C). This was probably because DOX and IR780 with positive charges partially shielded negative surface charges of DLMSNs during the drug loading period. Compared with DDI NPs, LM@DDI, PM@DDI and LPHM@DDI NPs showed evidently increased particle sizes, corresponding separately to 160.5 ± 10.8, 152.6 ± 10.6, and 153.9 ± 12.6 nm (Fig. 2B), and their zeta potentials also changed to −19.4 ± 3.2, −30.8 ± 4.3 and −26.9 ± 3.8 mV (Fig. 2C). These results confirmed that DDI NPs were successfully camouflaged with these cell membranes.

To evaluate the *in vitro* stability of LPHM@DDI NPs, their particle size and zeta potential changes were monitored within 5 d of storage in deionized water as well as in 10% FBS solution. The results are shown in Fig. 2D and E. The particle sizes of DLMSNs and DDI NPs increased gradually from the 3rd day in deionized water, but did not significantly change within 5 d in 10% FBS solution. Perhaps this was because DLMSNs and DDI NPs adsorbed serum proteins to form protein corona,

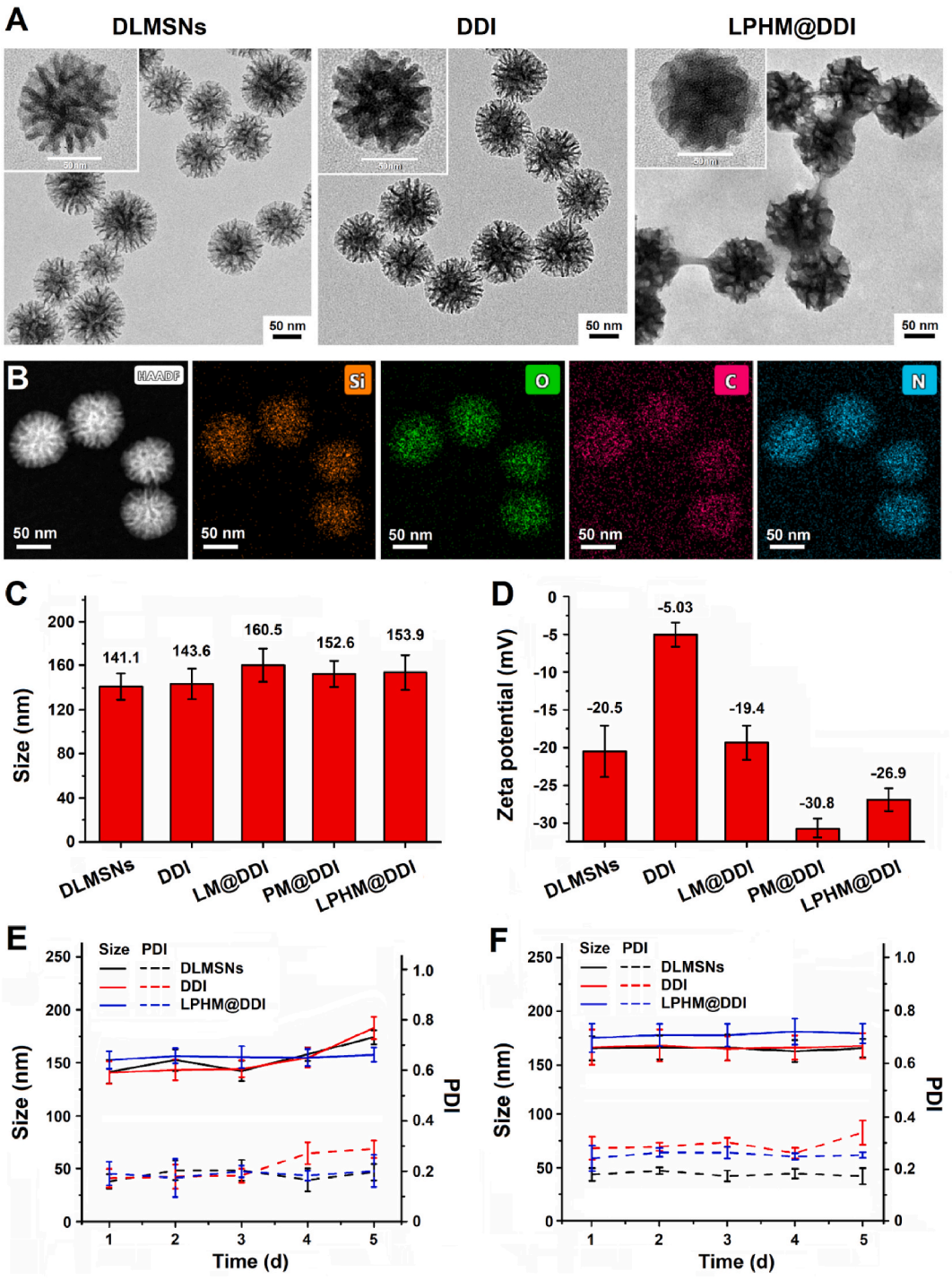

Fig. 2. Characterization and storage stability of LPHM@DDI NPs. (A) TEM images of DLMSNs, DDI and LPHM@DDI NPs. (B) EDS-mapping images of LPHM@DDI NPs with Si, O, C and N elements. Size distributions (C) and Zeta potentials (D) of DLMSNs, DDI, LM@DDI, PM@DDI, and LPHM@DDI NPs. Size and PDI changes of DLMSNs, DDI and LPHM@DDI NPs in deionized water (E) and 10% FBS solution (F).

thereby increasing their stability in 10% FBS solution. However, LPHM@DDI NPs exhibited relatively constant sizes and PDIs in both deionized water and 10% FBS solution within the whole storage period. This indicates that LPHM@DDI NPs have an excellent stability due to their surface coating with LPHM.

Given that the efficient retention of membrane proteins is a key factor for ensuring the cell membrane-camouflaged NPs to fully exert their biofunctions, we further analyzed the protein retention of LM and PM on LPHM@DLMSNs. First, the SDS-PAGE electrophoresis was applied to assess the protein components on LPHM@DLMSNs as compared to LM, PM, LM@DLMSNs, PM@DLMSNs, and DLMSNs. Coomassie bright blue-stained protein bands are shown in Fig. 3A. LM@DLMSNs and PM@DLMSNs displayed the same protein bands as those of LM and PM separately; but in the meantime, LPHM@DLMSNs showed the characteristic protein bands of both LM and PM. This meant that LPHM was successfully wrapped on the surfaces of DLMSNs and the membrane proteins were retained efficiently. Next, the immunofluorescence double staining method was employed to analyze the functional proteins (LFA-1 and P-selecin) on LM@DLMSNs, PM@DLMSNs and LPHM@DLMSNs. The results of flow cytometry confirmed the

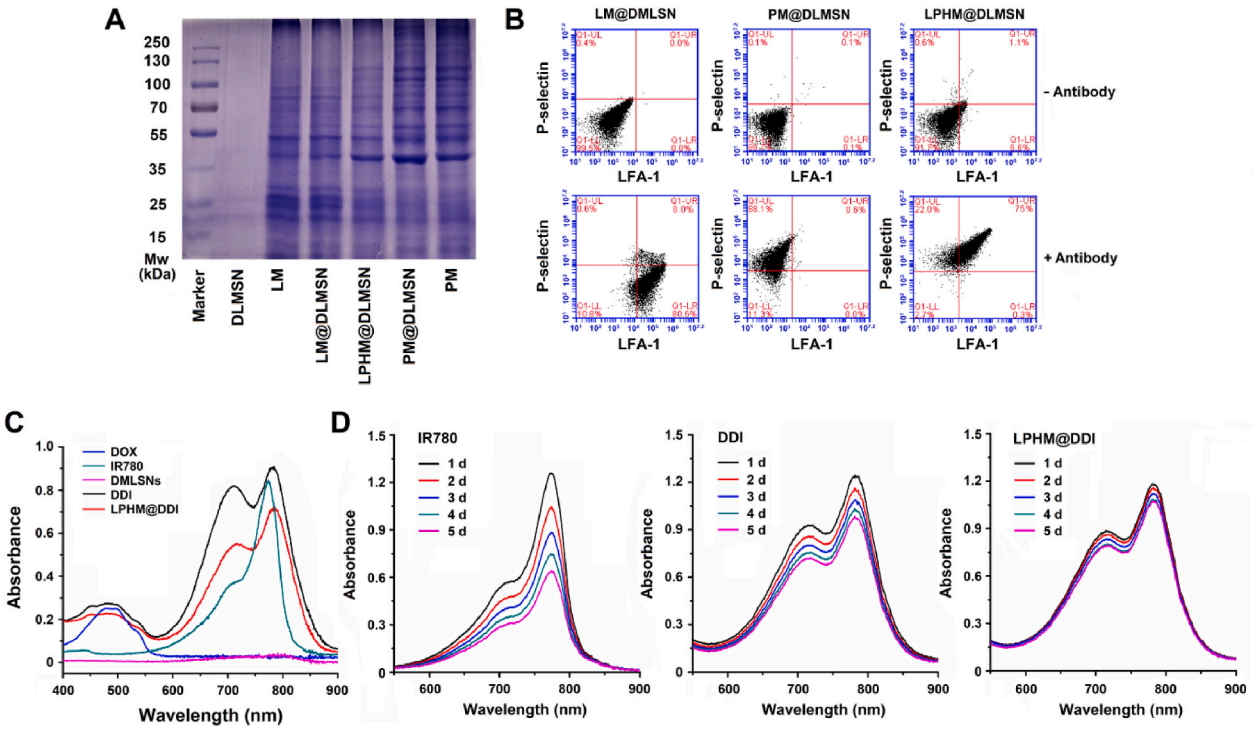

Fig. 3. Surface protein characterization and spectral features of LPHM@DDI NPs. (A) SDS-PAGE separation and Coomassie brilliant blue staining of the proteins isolated from DLMSNs, LM, LM@DLMSNs, PM, PM@DLMSNs, and LPHM@DLMSNs. (B) Flow cytometric analysis of LFA-1 and P-selectin on the surfaces of LM@DLMSNs, PM@DLMSNs and LPHM@DLMSNs. (C) UV–Vis–NIR absorption spectra of DOX, IR780, DDI NPs, and LPHM@DDI NPs. (D) Optical stabilities of IR780, DDI NPs and LPHM@DDI NPs during the 5-day storage period.

existence of these two proteins on the surfaces of LPHM@DLMSNs (Fig. 3B). It can be deduced that LPHM@DDI NPs should possess dual-targeting ability, including LFA-1/ICAM-1 interaction-dependent tumor vascular targeting and penetration ability and P-selectin/CD44 binding-mediated tumor cell targeting ability. This will be favorable for TNBC-targeted delivery of IR780 and DOX.

We also evaluated the spectral feature and optical stability of LPHM@DDI NPs. Fig. 3C shows the detected UV–Vis–NIR absorption spectra. DDI and LPHM@DDI NPs exhibited the characteristic absorption peaks of both IR780 and DOX, confirming the successful co-loading of these two therapeutic agents. However, there were obvious changes in the optical absorption spectra of DDI and LPHM@DDI NPs as compared to IR780, reflecting in a red shift of about 5 nm of the maximum absorption peak at 780 nm and a significantly enhanced absorbance at 712 nm. According to our previous report [14], this should be ascribed to the intermolecular interaction between IR780 and DOX and the polarity change of microenvironment around IR780. Fig. 3D shows the UV–Vis–NIR absorption spectra of IR780, DDI NPs and LPHM@DDI NPs during the 5-day storage period. IR780 exhibited poor optical stability and its absorption peak gradually decreased due to strong hydrophobic and fluorescence self-quenching characteristics, whereas DDI and LPHM@DDI NPs both greatly promoted the optical stability of IR780, indicating that the loading of IR780 with DLMSNs would help to improve its solubility and prevent its self-quenching. More importantly, LPHM@DDI NPs showed no obvious changes in their optical absorption spectra during storage, meaning that they might become a promising phototherapeutic agent.

3.2. *In vitro PTT/PDT performance and drug release behavior of LPHM@DDI NPs*

IR780 has been considered as an excellent PTT/PDT agent for tumor ablation, but its optical instability severely limits its effectiveness in thermal ablation [36]. The above results showed that LPHM@DDI NPs significantly promoted the optical stability of IR780, and thus they should have a higher photothermal/photodynamic performance than IR780. First, the PTT efficiencies of IR780, DDI NPs and LPHM@DDI NPs were compared by monitoring their temperature elevation effects during 808 nm laser irradiation with an intensity of 2 W/cm^2 for 10 min. The IR thermal images of various samples and their temperature change curves are displayed separately in Fig. 4A and B. IR780 exhibited an obvious temperature-elevation effect, e.g., the temperature rapidly increased to 46 °C and followed by gradually dropping to 34 °C during the whole laser irradiation period. By comparison, DDI and LPHM@DDI NPs had significantly improved PTT efficiencies, as evidenced by their temperature enhancements to above 55 °C within the first 5 min. And after that, the temperature of DDI NPs began to drop, while LPHM@DDI NPs maintained a relatively constant temperature in the subsequent 5 min. This might be owing to the fact that LPHM efficiently prevented the opening cores and delayed the release of IR780 from DLMSNs. Thus it can be seen that LPHM@DDI NPs is a promising PTT agent for cancer ablation.

The PDT efficiencies of IR780, DDI NPs and LPHM@DDI NPs were compared through assessing the generation levels of ROS after different times of 808 nm laser irradiation with an intensity of 2 W/cm^2 by using SOSG as a fluorescence probe. As shown in Fig. 4C, IR780, DDI NPs and LPHM@DDI NPs all notably enhanced the ROS levels in their solutions within the first 4 min of laser irradiation, while DDI and LPHM@DDI NPs displayed much stronger promotion effects on the ROS generation than IR780. This demonstrated that IR780 loaded by DDI and LPHM@DDI NPs had a higher PDT efficiency owing to its improved optical stability. The PDT efficiencies of the above phototherapeutic agents were also compared in 4T1 cells by evaluating the productions of intracellular ROS using DCFH-DA as a fluorescence probe. As shown in Fig. S2, the intensive green fluorescence was clearly visible in the cells after incubation with IR780, DDI NPs and LPHM@DDI NPs upon laser irradiation, indicating the intracellular productions of ROS. The flow cytometry was further used to detect quantitatively the production

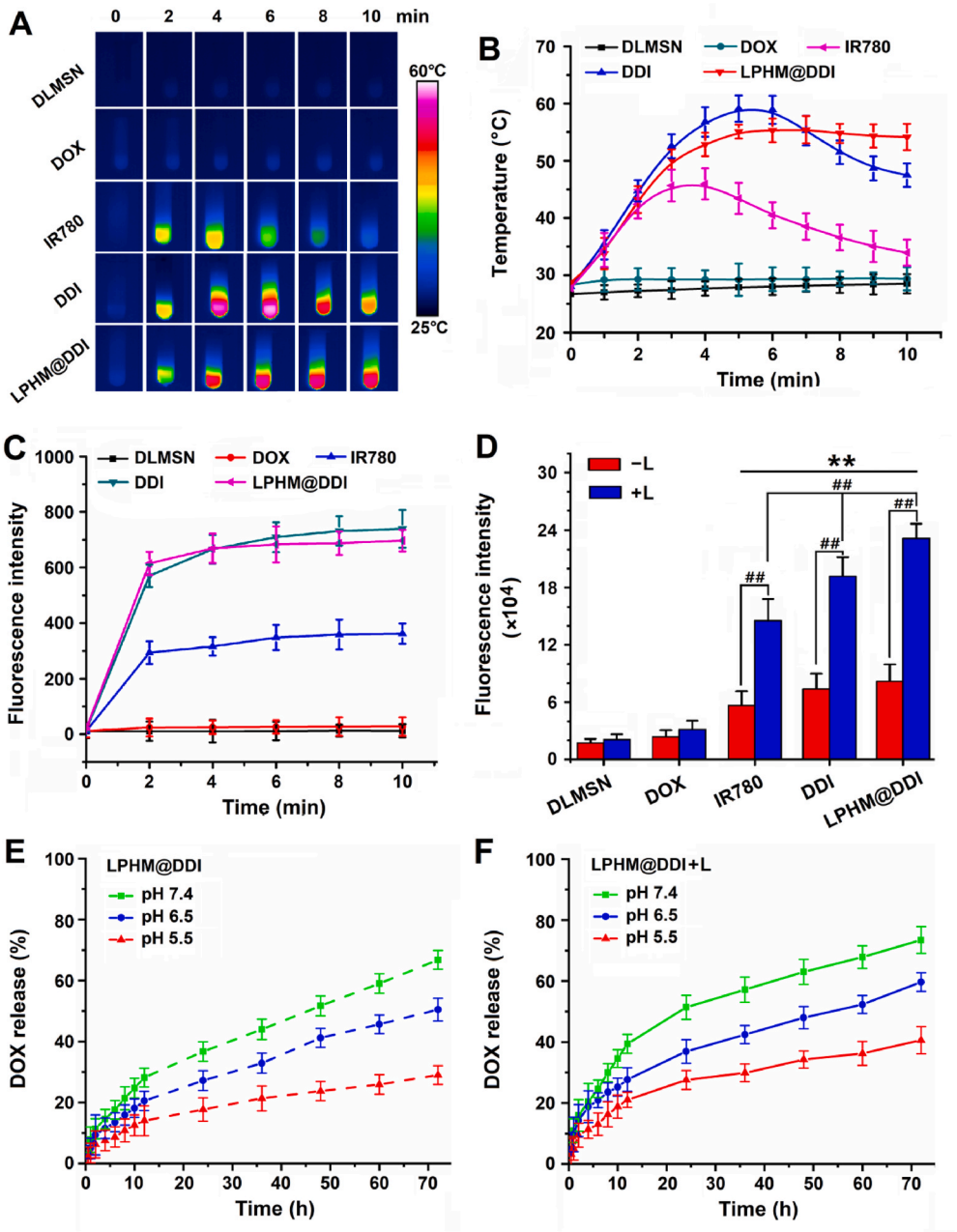

Fig. 4. *In vitro* PTT/PDT performances and drug releases of LPHM@DDI NPs. IR thermal images of DLMSNs, DOX, IR780, DDI NPs, and LPHM@DDI NPs (A) and their temperature changes (B) within the 10-min laser irradiation period. (C) Fluorescence intensities of SOSG in the dispersions of DLMSNs, DOX, IR780, DDI NPs, and LPHM@DDI NPs after 2, 4, 6, 8, and 10 min of laser irradiation. (D) Fluorescence intensities of DCFH-DA in 4T1 cells after incubation of IR780, DOX, DDI NPs, and LPHM@DDI NPs alone (–L) and followed by laser irradiation (+L). ** represents $P < 0.01$ vs. control; ## represents $P < 0.01$ between two groups. (E) *In vitro* release profiles of DOX from LPHM@DDI NPs alone and (F) their pre-procession with 10-min laser irradiation at different pH values.

levels of ROS in these cells and the results are shown in Fig. 4D. Upon laser irradiation, DDI and LPHM@DDI NPs also exhibited more obvious promotion effects on the intracellular ROS production as compared to IR780, confirming their strong PDT potency. LPHM@DDI NPs possessed a remarkedly higher PDT efficiency than DDI NPs, which should be ascribed to their specific cellular internalization mediated by P-selectin/CD44 binding. All above results indicate that LPHM@DDI NPs might be a promising photosensitizer for cancer PDT.

The PTT/PDT effects of LPHM@DDI NPs can enhance the permeability of LPHM and thus will promote the release of DOX. In the present study, we compared the *in vitro* releases of DOX from LPHM@DDI NPs and their preprocessing with laser irradiation at different pH values. Owing to the preventing effect of LPHM on the pore openings of DLMSNs, DOX exhibited the clearly sustained releases from LPHM@DDI NPs (Fig. 4E). As expected, the laser irradiation significantly enhanced the release rates of DOX from LPHM@DDI NPs (Fig. 4F). At 72 h, the accumulative release amounts of DOX were 73.5 ± 4.4%, 60.6 ± 3.1% and 40.6 ± 5.5% at pH 5.5, pH 6.5 and pH 7.4, separately; but in the meantime, only 66.8 ± 2.9%, 50.5 ± 3.7% and 29.1 ± 3.1% of DOX were released from LPHM@DDI NPs. DDI and LPHM@DDI NPs both showed an evident pH-responsive drug release behavior, e.g., the release rates of DOX were gradually accelerated with the decrease of pH value from 7.4 to 5.5. All these results demonstrate that LPHM@DDI NPs possess photo/pH dual-responsive drug release behavior, which will facilitate the controlled release of DOX in the weakly acidic tumor microenvironment.

3.3. Cellular uptakes of LPHM@DDI NPs in TNBC cells and macrophages

As P-selectin expressed on PM is a natural ligand for CD44 [35], we hold the opinion that LPHM@DDI NPs can be uptaken efficiently by 4T1 cells that have been verified to overexpress CD44 in our previous report [37]. Therefore, we investigated the specific uptake of LPHM@DDI NPs by 4T1 cells in comparison with DDI, LM@DDI and PM@DDI NPs.

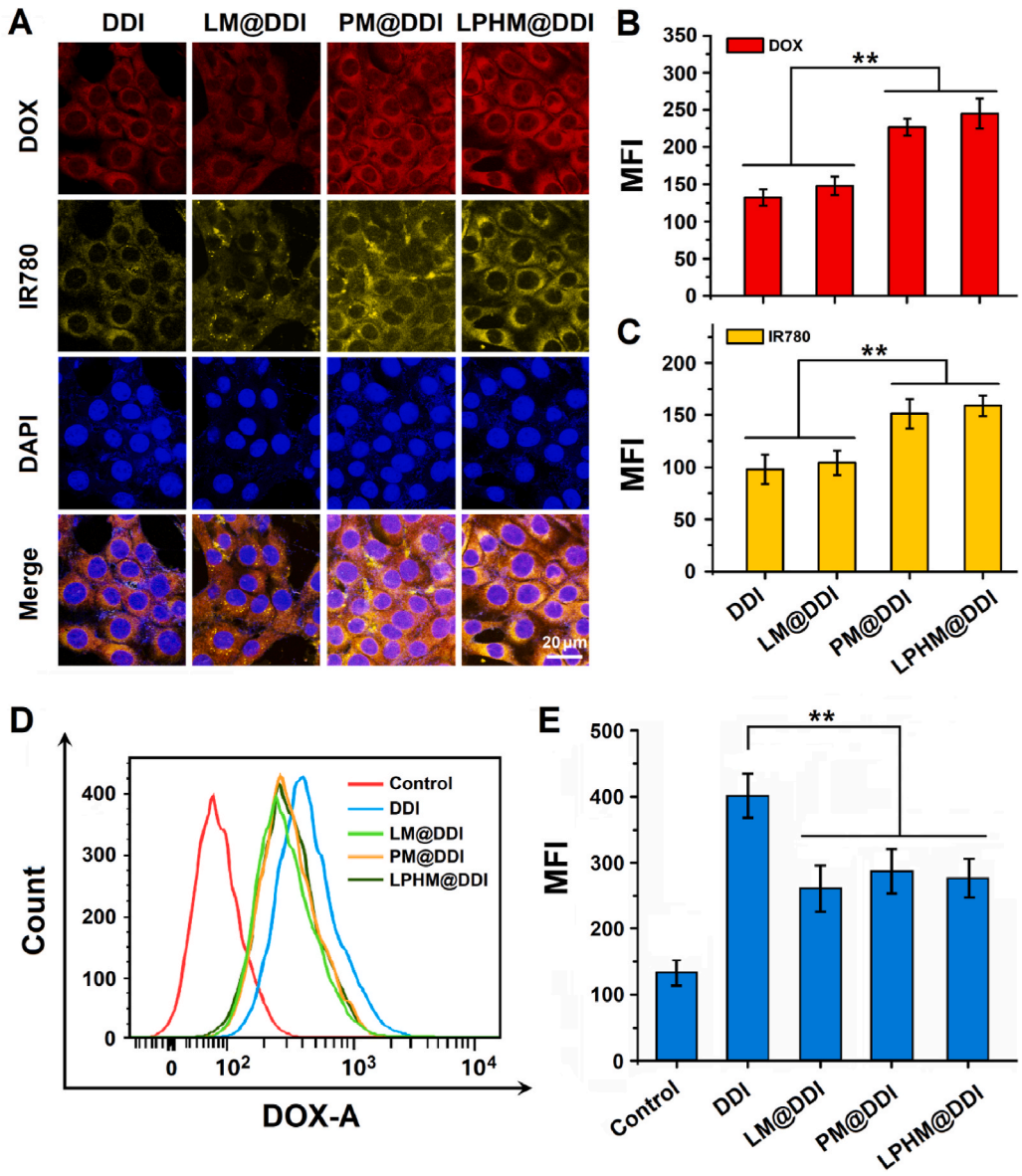

Fig. 5. Cellular uptake and intracellular localization of LPHM@DDI NPs. (A) Confocal microscopic images of 4T1 cells after 2 h of incubation with DDI, LM@DDI, PM@DDI, and LPHM@DDI NPs. Mean fluorescence intensities (MFIs) of DOX (B) and IR780 (C) in 4T1 cells after incubation with the above NPs. Flow cytometry analysis of Raw 264.7 cells after 1 h of incubation of DDI, LM@DDI, PM@DDI and LPHM@DDI NPs (D) and MFIs of intracellular DOX (E). ** represents $P < 0.01$ vs. control.

Fig. 5A shows the confocal microscopic images of the cells after 2 h of incubation with these NPs. DOX and IR780 were mainly localized in the cytoplasm and mostly overlapped to exhibit yellow fluorescence in the merged images, demonstrating that they were delivered into the cells through cellular internalization of these NPs. PM@DDI and LPHM@DDI NPs showed significantly stronger fluorescence signals of both DOX and IR780 than DDI and LM@DDI NPs, while no evident differences were observed between the fluorescence signals from PM@DDI and LPHM@DDI NPs (Fig. 5B and C). These results indicate that the P-selectin/CD44 binding can mediate the specific cellular internalization of PM@DDI and LPHM@DDI NPs in 4T1 cells.

It is well known that the cell membrane-camouflage can help NPs to escape from the immune system and hence prolong their plasma circulation time [25–28]. Therefore, we further compared the phagocytosis ability of mouse macrophage Raw 264.7 cells for DDI, LM@DDI, PM@DDI, and LPHM@DDI NPs using the flow cytometry, thus to preliminarily evaluate the escape capability of LPHM@DDI NPs from the immune system. After incubation for 1 h, LM@DDI, PM@DDI and LPHM@DDI NPs all notably reduced the cellular uptakes of DOX in Raw 264.7 cells as compared to DDI NPs (Fig. 5D and E), demonstrating that these cell membrane-camouflaged NPs significantly escaped from the phagocytosis of macrophages. These results were basically consistent with other biomimetic NPs camouflaged with leukocyte and platelet membranes as previously reported [33,35].

3.4. Synergistic cytotoxicity and apoptosis-inducing activity mediated by LPHM@DDI NPs

According to the above results, LPHM@DDI NPs have strong PTT/PDT performances, specific cellular uptake characteristics and greatly accelerated drug release behavior upon laser irradiation, thereby advantaging TNBC combination treatment. Subsequently, we investigated the *in vitro* synergistic effects of LPHM@DDI NP-mediated PTT/PDT combined with chemotherapy against TNBC. First, their synergistic cytotoxicity in 4T1 cells was assessed by the MTT assay. The influence of laser irradiation on the cell growth was not observed and nearly 95% of the cells survived. With and without laser irradiation, DOX had almost identical cytotoxicities (Fig. 6A). However, IR780 and the DOX/IR780 mixture showed notably higher cytotoxicity upon laser irradiation than their treatments alone (Fig. 6B and C). The DOX/IR780 mixture upon laser irradiation exerted the synergistic cytotoxicity of PTT/PDT and chemotherapy, reflecting in that the CI values at different drug

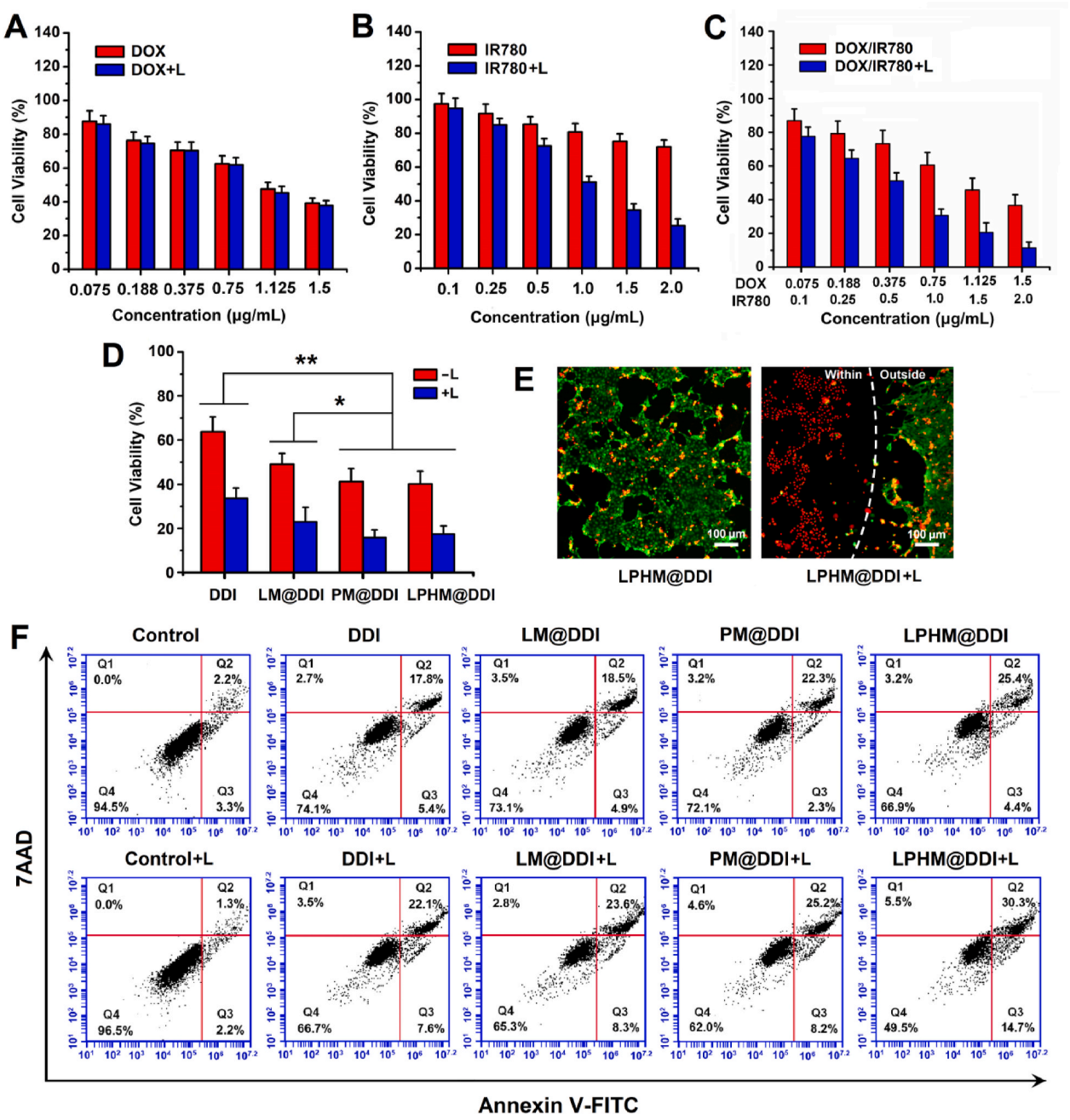

Fig. 6. *In vitro* synergistic anti-TNBC effects of LHPM@DDI NP-mediated combination treatment. Cytotoxicities of DOX with and without laser irradiation (A), IR780 with and without laser irradiation (B), and DDI NPs with and without laser irradiation (C) in 4T1 cells at different drug concentrations. (D) Cytotoxicities of DDI, LM@DDI, PM@DDI, and LPHM@DDI NPs with and without laser irradiation at the DOX and IR780 concentrations of 0.75 and 1.0 μg/mL, respectively. * and ** represent $P < 0.05$ and $P < 0.01$ between two groups. (E) Fluorescence microscopic images of 4T1 cells treated with LPHM@DDI NPs alone and followed by laser irradiation after co-staining of calcein-AM and ethidium homodimer-1. Green and red fluorescence indicate liver and dead cells. (F) Flow cytometry analysis of apoptosis in 4T1 cells treated with DDI, LM@DDI, PM@DDI, and LPHM@DDI NPs alone and followed by laser irradiation. The DOX and IR780 concentrations were 0.45 and 0.6 μg/mL, respectively. Four quadrants (Q1, Q2, Q3 and Q4) represent dead cells, late apoptotic cells, early apoptotic cells and live cells, respectively.

concentrations were smaller than 1.0 as compared to DOX and IR780 upon laser irradiation (Fig. S3A and S3B). We further compared the inhibitory efficacies of DDI, LM@DDI, PM@DDI, and LPHM@DDI NPs on the cell growth when the DOX and IR780 concentrations were 0.75 and 1.0 μg/mL. PM@DDI and LPHM@DDI NPs exhibited almost identical inhibitory activities, which were significantly stronger than those of DDI and LM@DDI NPs either with or without laser irradiation (Fig. 6D). This was because PM and LPHM promoted the uptakes of PM@DDI and LPHM@DDI NPs by 4T1 cells through the specific binding of P-selectin/CD44.

The synergistic cytotoxicity of LPHM@DDI NP-mediated combination treatment in 4T1 cells was also detected visibly using the LIVE/DEAD cell staining. The fluorescence microscopic images of the stained cells in different treatment groups are displayed in Fig. 6E. *Green and red* fluorescence indicated the l*ive and dead cells* separately. After 12-h incubation with LPHM@DDI NPs, only a few cells died due to the cytotoxic effect of released DOX. Upon laser irradiation, LPHM@DDI NPs killed the cells within the laser spot, while the cells outside the laser spot survived mostly, similar to those under non-laser irradiation. This demonstrated that LPHM@DDI NPs exerted synergistic cell-king activity

through the combination of PTT/PDT with chemotherapy. We also evaluated the synergistic inducing activity of LPHM@DDI NP-mediated combination treatment on the apoptosis of 4T1 cells and the flow cytometry data are displayed in Fig. 6F. The cells in the treatment group of LPHM@DDI NPs with laser irradiation exhibited the highest apoptosis rate, further verifying the synergistic anti-TNBC effect of PTT/PDT and chemotherapy *in vitro*.

3.5. Biodistribution and tumor-accumulation of LPHM@DDI NPs in TNBC mice

A mouse TNBC model was constructed through inoculation of 4T1 cells into the groin of female BALB/c mice and then applied to evaluate the biodistribution and tumor-accumulation of LPHM@DDI NPs by observing the fluorescence of IR780. Fig. 7A shows the *in vivo* fluorescence images of the TNBC model mice at different times after injection of DDI, LM@DDI, PM@DDI, and LPHM@DDI NPs via tail vein. At 6 h afterwards, the fluorescence signals from these NPs were located mainly in the liver and the tumor, indicating that these NPs reached tumor site through the enhanced permeability and retention (EPR) effect. At 12 h post-administration, the liver fluorescence was reduced significantly in all NP-treated mice. At 48 h post-administration, only the tumor fluorescence was clearly visible, and the fluorescence signals sourced from LM@DDI, PM@DDI and LPHM@DDI NPs were much stronger than that of DDI NPs. This might be owing to the fact that the cell membrane-camouflage prolonged the blood circulation time of NPs and thus promoted their tumor-accumulation. Fig. 7B and C shows the fluorescence microscopic images of major organs as well as tumors isolated from the above mice and the quantitative analysis of tissue fluorescence. Compared with LM@DDI and PM@DDI NPs, LPHM@DDI NPs exhibited significantly reduced distribution in the liver and enhanced accumulation in the tumor. And furthermore, LPHM@DDI NPs also exhibited the slowest fluorescence attenuation rate at tumor site (Fig. S4). All these results confirmed that LPHM@DDI NPs had an excellent tumor-targeting performance due to the mediation of LPHM. First, the activation of the LFA-1/ICAM-1 adhesion pathway can increase tumor vascular permeability as previously reported [33], thus boosting the penetration of LPHM@DDI NPs through tumor vessels. Second, the P-selectin/CD44 specific binding can promote the accumulation of LPHM@DDI NPs at the tumor site.

3.6. In vivo PTT/PDT performance of LPHM@DDI NPs

4T1 tumor-bearing mice were injected with the DOX/IR780 mixture, DDI NPs, LM@DDI NPs, PM@DDI NPs, and LPHM@DDI NPs via tail vein, and 12 h later received the 808 nm laser irradiation with an intensity of 2 W/cm^2 at tumor site for 10 min. During the laser irradiation period, the PTT efficiencies of these NPs were compared through monitoring the tumor temperature changes. The IR thermal images of the mice and the heating curves of the tumors are displayed respectively in Fig. 8A and B. Compared to the control, all these phototherapeutic agents showed very strong *in vivo* PTT efficiencies, whereas DDI, LM@DDI, PM@DDI, and LPHM@DDI NPs exerted more stable temperature elevation effect than the DOX/IR780 mixture due to their enhanced optical stability. These NPs raised the tumor temperatures gradually within the first 5 min of laser irradiation and then maintained

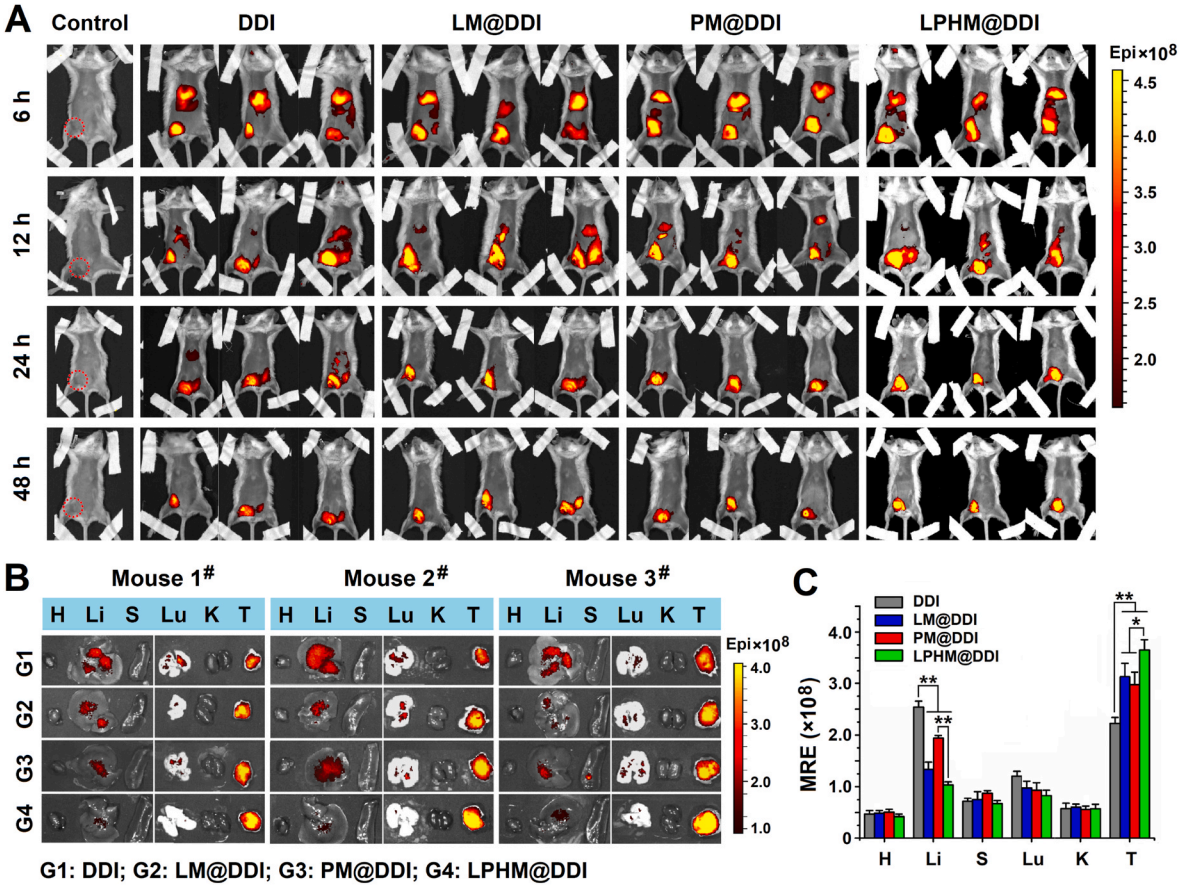

Fig. 7. Biodistribution and tumor accumulation of LPHM@DDI NPs in TNBC mice. (A) *In vivo* fluorescence images of 4T1 tumor-bearing mice at 6, 12, 24 and 48 h post-administration of PBS (the control), DDI NPs, LM@DDI NPs, PM@DDI NPs, and LPHM@DDI NPs. The dotted-red circle represents the tumor location in the control mouse. Ex vivo fluorescence images (B) and mean radiant efficiencies (MREs) (C) of the major organs and tumors isolated from the above mice. H, Li, S, Lu, K and T indicate the heart, liver, spleen, lung, kidney and tumor, respectively. * and ** represent $P < 0.05$ and $P < 0.01$ between two groups.

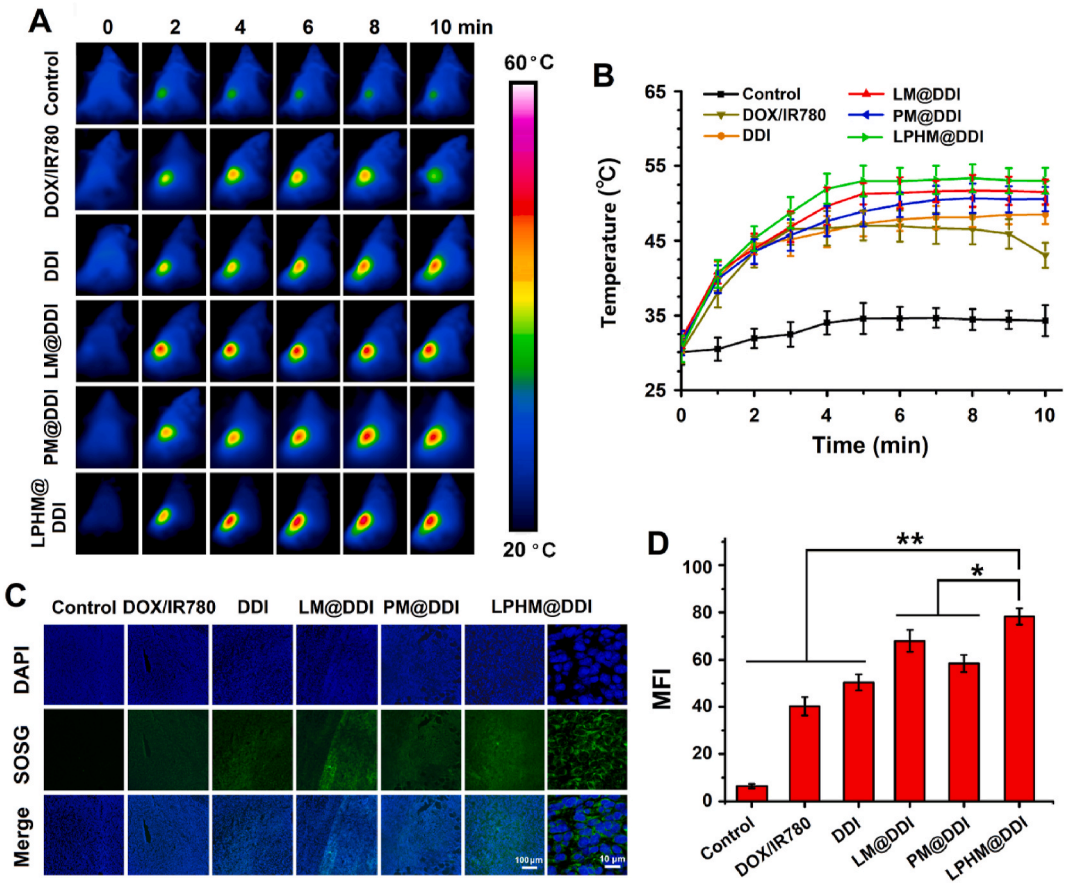

Fig. 8. *In vivo* PTT/PDT performances of LPHM@DDI NPs. IR thermal images of 4T tumor-bearing mice with intravenous injection of PBS (the control), DOX/IR780 mixture, DDI NPs, LM@DDI NPs, PM@DDI NPs, and LPHM@DDI NPs (A) and their tumor temperature changes (B) during a 10 min period of laser irradiation at tumor site. Fluorescence microscopic images of tumor sections sourced from the above treated mice after processing with SOSG (C) and the comparison of their MFIs (D). * and ** represent $P < 0.05$ and $P < 0.01$ between two groups.

at relative constant temperatures. By comparison, LPHM@DDI NPs exhibited the highest PTT efficiency and quickly raised the tumor temperature to exceed 50 °C, which should be owing to the dual-targeting ability of LPHM@DDI NPs for TNBC.

SOSG was applied as a fluorescence probe to evaluate the generation levels of ROS in the tumors from the mice bearing 4T1 tumors with different times of laser irradiation. The fluorescence microscopic images of tumor sections and the comparison for their fluorescence intensities are shown separately in Fig. 8C and D. Nearly no fluorescence was visible in the tumor of the control mouse. Whereas, upon laser irradiation, the intensive green fluorescence was visible clearly in the tumors of the mice administrated with the DOX/IR780 mixture, DDI NPs, LM@DDI NPs, PM@DDI NPs, and LPHM@DDI NPs. It indicated that these phototherapeutic agents exerted their PDT efficiencies to promote the ROS generations greatly. LPHM@DDI NPs also displayed the highest PDT efficiency. All above results suggest that LPHM@DDI NPs can be applied for TNBC treatment as a promising phototherapeutic agent.

3.7. *In vivo* antitumor effects of LPHM@DDI NPs-mediated combination treatment

4T1 tumor-bearing mice were used to evaluate the *in vivo* synergistic effects of LPHM@DDI NP-mediated combination treatment. The DOX/IR780 mixture, DDI NPs, LM@DDI NPs, PM@DDI NPs, and LPHM@DDI NPs were administrated via intravenous injection and the 808 nm laser irradiation with an intensity of 2 W/cm^2 was performed at tumor site for 5 min at 12 h post administration. All treatments were performed only once with 21-day period and the tumor volumes of the treated mice were monitored continuously. Fig. 9A and B displays the tumor growth curves. Compared to the control group, the tumors in all non-laser irradiation treatment groups exhibited slightly slower growth rates within the first 10 d and afterwards grew quickly. This was because DOX released from these formulations exerted chemotherapeutic action to a certain extent at a relatively low dose of 1.5 mg/kg. However, upon laser irradiation, these phototherapeutic agents all remarkably inhibited on the tumor growth, e.g., the tumors in the treated mice were almost completely suppressed within the first 10 d. It demonstrated that IR780 in these agents exerted the PTT/PDT performances on tumor ablation. Starting from the 10th day upon laser irradiation, the tumors of the mice administrated with the DOX/IR780 mixture and DDI NPs began to recur and grew quickly, while the tumor growth was slowed down notably in the mice with administration of LM@DDI, PM@DDI and LPHM@DDI NPs. This might be due to the prolonged circulation and tumor-targeted delivery of NPs camouflaged with LM, PM and LPHM, and the accelerated release of DOX from these NPs after laser irradiation. Among all the treated mice, the mice receiving LPHM@DDI NP-mediated combination treatment of PTT/PDT with chemotherapy had the smallest tumor volumes (Fig. 9C and Fig. S5A). Furthermore, the microscopic images of tumor sections with H&E staining (Fig. 9D) and the photos of the mice at 0, 5 and 18 d during the treatment period (Fig. 9E) also revealed that LPHM@DDI NP-mediated combination treatment inhibited tumor recurrence efficiently.

In the meantime, the changes in body weights of the treated mice were also detected and the data are shown in Fig. 9F and G. All the treated mice exhibited only slightly decreased body weights within the initial 4 d due to the stimulation of laser irradiation, but no significant

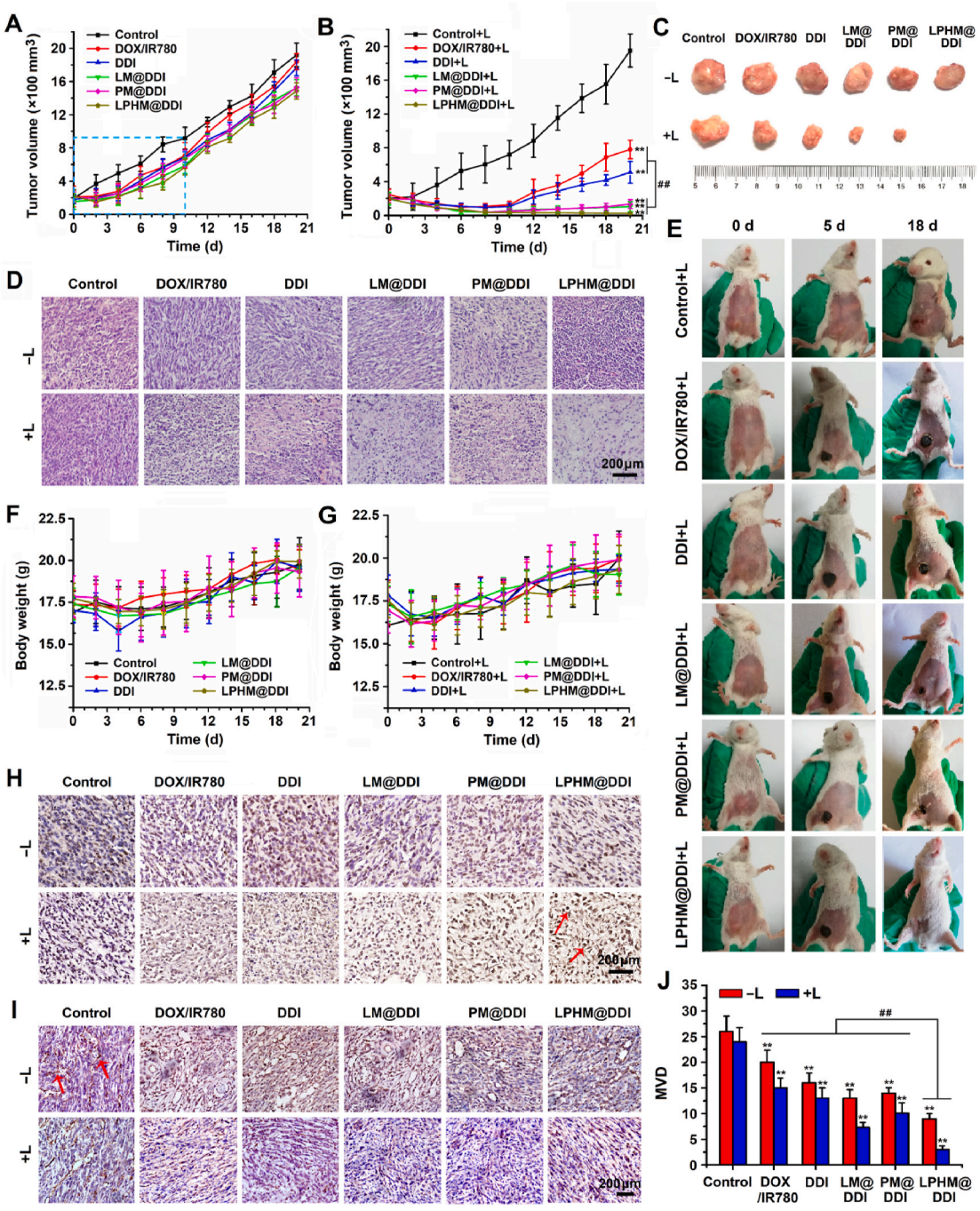

Fig. 9. *In vivo* synergistic anti-TNBC effects of LPHM@DDI NP-mediated combination treatment. Tumor growth curves of 4T1 tumor-bearing mice treated with PBS (the control), the DOX/IR780 mixture, DDI NPs, LM@DDI NPs, PM@DDI, and LPHM@DDI NPs alone (A) and followed by laser irradiation (B). Photos of representative tumors sourced from the mice with various treatments (C) and microscopic images of their sections with H&E staining (D). (E) Photos of representative mice at 0, 5 and 18 d during the treatment period. Weight change curves of the mice receiving the above-mentioned treatments (F) and followed by laser irradiation (G). Microscopic images of tumor sections with TUNEL staining (H) and CD31 immunohistochemical staining (I) from the mice at 2 d during treatment period. The red arrows represent apoptotic cells or CD31-stained areas in tumor sections. (J) Comparison of MVDs calculated from CD31-stained tumor sections in various treatment groups. ** represents $P < 0.01$ vs. control; ## represents $P < 0.01$ between two groups.

difference was observed in their body weights as compared to the control mice. Moreover, no evident pathological damages were observed in the major organs including heart, liver, spleen, lung, and kidney in these treated mice (Fig. S5B). This should be ascribed to the following two factors. First, the doses of DOX and IR780 in these treatments were only 1.5 and 2.0 mg/kg, respectively, and hence will not bring any damage to the mice. Second, the tumor-targeted delivery mediated by DDI, LM@DDI, PM@DDI, and LPHM@DDI NPs will alleviate the toxicity of DOX and IR780. Thus it can be deduced that PLHM@DDI NP-mediated combination treatment of PTT/PDT with chemotherapy has a high-level biosafety for *in vivo* TNBC therapy.

At 2 d after various treatments, the tumor tissues sourced from the treated mice were processed with TUNEL staining and CD31 immunohistochemical staining, thus assessing tumor apoptosis and tumor angiogenesis separately. As shown in Fig. 9H, the DOX/IR780 mixture, DDI, LM@DDI, PM@DDI, and LPHM@DDI NPs all notably induced the

apoptosis of tumor cells after laser irradiation, demonstrating that IR780 in these formulations exerted the PTT/PDT performance on tumor ablation. By comparison, LPHM@DDI NPs exhibited a much stronger apoptosis-inducing activity than other treatments upon laser irradiation, e.g., the tumor cells were almost completely apoptotic in the treated mice. This experimental result was basically coincided with the above H&E staining results of tumor sections (Fig. 9D), showing that tumor necrosis was more obvious in the mice after treatment of LPHM@DDI NPs and laser irradiation. These results demonstrate that LPHM@DDI NPs can directly damage tumor cells though efficient combination of PTT/PDT with chemotherapy. Fig. 9I shows the microscopic images of tumor sections with CD31 immumohistochemical staining. Large microvessels were clearly observed in the tumors in the treatment groups of DOX/IR780 mixture, DDI, LM@DDI, PM@DDI, and LPHM@DDI NPs, but mostly disappeared in the treatment groups of these phototherapeutic agents with laser irradiation. MVDs in tumor sections were further counted and the results are shown in Fig. 9J. Even without laser irradiation, all these phototherapeutic agents displayed significant suppression effects on tumor angiogenesis as compared to the control. This should be owing to the toxicity of released DOX on the vascular endothelial cells. Upon laser irradiation, their suppression efficacies were further enhanced significantly, indicating that PTT/PDT mediated by these phototherapeutic agents can efficiently destroy tumor neovasculature. By comparison, LPHM@DDI NPs also exhibited the highest destroying activity whether with or without laser irradiation due to their dual-targeting ability for delivering DOX and IR780. From the above results, it can be seen that LPHM@DDI NPs-mediated combination treatment of PTT/PDT with chemotherapy can inhibit tumor growth and recurrence indirectly through suppressing tumor angiogenesis.

4. Conclusions

In summary, a novel biomimetic nanoplatform was developed in this study by taking advantages of the large pore size of DLMSNs and the camouflage of LPHM for efficient co-loading and tumor-targeted delivery of IR780 and DOX, thus achieving the synergistic effects of PTT/PDT and chemotherapy against TNBC. The obtained LPHM@DDI NPs had an excellent TNBC-targeting ability and very high *in vitro* and *in vivo* PTT/PDT performances. LPHM@DDI NP-mediated combination treatment obtained synergistic cytotoxicity and apoptosis-inducing activity in TNBC cells, and also notably suppressed tumor growth and recurrence in TNBC mice through tumor ablation and antiangiogenesis. It thus can be seen that this study provides a promising biomimetic nanoplatform for the combination treatment of PTT/PDT with chemotherapy against TNBC. Of course, this nanoplatform can be applied equally to other CD44-overexpressing cancers.

CRediT authorship contribution statement

Tao Zhang: Conceptualization, Methodology, Software, Data curation, Writing – original draft. **Hui Liu:** Methodology, Software, Data curation, Writing – original draft. **Ling Li:** Visualization, Methodology, Data curation, Writing – original draft. **Zhaoyang Guo:** Methodology, Data curation. **Jia Song:** Methodology, Data curation. **Xiaoying Yang:** Resources, Funding acquisition. **Guoyun Wan:** Methodology. **Rongshan Li:** Conceptualization, Methodology, Data curation, Writing – review & editing. **Yinsong Wang:** Writing – review & editing, Supervision, Funding acquisition, Project administration.

Declaration of competing interest

There is no conflict of interest.

Acknowledgements

This work was financially supported by the National Natural Science Foundation of China (Nos. 81972903, 12074284 and 81803101), the Natural Science Foundation of Tianjin City of China (Nos. 18JCZDJC33400 and 19JCQNJC12300), and the Excellent Talent Project of Tianjin Medical University.

Appendix A. Supplementary data

Supplementary data related to this article can be found at https://doi.org/10.1016/j.bioactmat.2021.04.004.

References

[1] P. Sharma, Biology and management of patients with triple-negative breast cancer, Oncol. 21 (9) (2016) 1050–1062.
[2] G. Bianchini, J.M. Balko, I.A. Mayer, M.E. Sanders, L. Gianni, Triple-negative breast cancer: challenges and opportunities of a heterogeneous disease, Nat. Rev. Clin. Oncol. 13 (11) (2016) 674–690.
[3] M. Nedeljković, A. Damjanović, Mechanisms of chemotherapy resistance in triple-negative breast cancer-how we can rise to the challenge, Cells 8 (9) (2019) 957.
[4] A. Marra, G. Viale, G. Curigliano, Recent advances in triple negative breast cancer: the immunotherapy era, BMC Med. 17 (1) (2019) 90.
[5] E.A. Mittendorf, A.V. Philips, F. Meric-Bernstam, N. Qiao, Y. Wu, S. Harrington, X. Su, Y. Wang, A.M. Gonzalez-Angulo, A. Akcakanat, A. Chawla, M. Curran, P. Hwu, P. Sharma, J.K. Litton, J.J. Molldrem, G. Alatrash, PD-L1 expression in triple-negative breast cancer, Cancer Immunol. Res. 2 (4) (2014) 361–370.
[6] X. Li, J.F. Lovell, J. Yoon, X. Chen, Clinical development and potential of photothermal and photodynamic therapies for cancer, Nat. Rev. Clin. Oncol. 17 (11) (2020) 657–674.
[7] S. Roy, B.L. Tony, Phototherapy in cancer prevention and treatment, J. Cancer Prev. Curr. Res. 7 (1) (2017), 00224.
[8] D.E. Dolmans, D. Fukumura, R.K. Jain, Photodynamic therapy for cancer, Nat. Rev. Canc. 3 (2003) 380–387.
[9] X. Hou, Y. Tao, Y. Pang, X. Li, G. Jiang, Y. Liu, Nanoparticle-based photothermal and photodynamic immunotherapy for tumor treatment, Int. J. Canc. 143 (12) (2018) 3050–3060.
[10] N. Plenagl, L. Duse, B.S. Seitz, N. Goergen, S.R. Pinnapireddy, J. Jedelska, J. Brüßler, U. Bakowsky, Photodynamic therapy - hypericin tetraether liposome conjugates and their antitumor and antiangiogenic activity, Drug Deliv. 26 (1) (2019) 23–33.
[11] A. Yuan, J. Wu, X. Tang, L. Zhao, F. Xu, Y. Hu, Application of near-infrared dyes for tumor imaging, photothermal, and photodynamic therapies, J. Pharm. Sci. 102 (1) (2013) 6–28.
[12] G. Wan, B. Chen, L. Li, D. Wang, S. Shi, T. Zhang, Y. Wang, L. Zhang, Y. Wang, Nanoscaled red blood cells facilitate breast cancer treatment by combining photothermal/photodynamic therapy and chemotherapy, Biomaterials 155 (2018) 25–40.
[13] M. Lu, N. Kang, C. Chen, L. Yang, Y. Li, M. Hong, X. Luo, L. Ren, X. Wang, Plasmonic enhancement of cyanine dyes for near-infrared light-triggered photodynamic/photothermal therapy and fluorescent imaging, Nanotechnology 28 (44) (2017) 445710.
[14] G. Wan, Y. Cheng, J. Song, Q. Chen, B. Chen, Y. Liu, S. Ji, H. Chen, Y. Wang, Nucleus-targeting near-infrared nanoparticles based on TAT peptideconjugated IR780 for photo-chemotherapy of breast cancer, Chem. Eng. J. 380 (2020) 122458.
[15] D. Wang, S. Zhang, T. Zhang, G. Wan, B. Chen, Q. Xiong, J. Zhang, W. Zhang, Y. Wang, Pullulan-coated phospholipid and Pluronic F68 complex nanoparticles for carrying IR780 and paclitaxel to treat hepatocellular carcinoma by combining photothermal therapy/photodynamic therapy and chemotherapy, Int. J. Nanomed. 12 (2017) 8649–8670.
[16] Z. Xie, T. Fan, J. An, W. Choi, Y. Duo, Y. Ge, B. Zhang, G. Nie, N. Xie, T. Zheng, Y. Chen, H. Zhang, J.S. Kim, Emerging combination strategies with phototherapy in cancer nanomedicine, Chem. Soc. Rev. 49 (22) (2020) 8065–8087.
[17] F. Tang, L. Li, D. Chen, Mesoporous silica nanoparticles: synthesis, biocompatibility and drug delivery, Adv. Mater. 24 (12) (2012) 1504–1534.
[18] Y. Wang, Q. Zhao, N. Han, L. Bai, J. Li, J. Liu, E. Che, L. Hu, Q. Zhang, T. Jiang, S. Wang, Mesoporous silica nanoparticles in drug delivery and biomedical applications, Nanomedicine 11 (2) (2015) 313–327.
[19] M.H. Kim, H.K. Na, Y.K. Kim, S.R. Ryoo, H.S. Cho, K.E. Lee, H. Jeon, R. Ryoo, D. H. Min, Facile synthesis of monodispersed mesoporous silica nanoparticles with ultralarge pores and their application in gene delivery, ACS Nano 5 (5) (2011) 3568–3576.
[20] D. Kwon, B.G. Cha, Y. Cho, J. Min, E.B. Park, S.J. Kang, J. Kim, Extra-large pore mesoporous silica nanoparticles for directing in vivo M2 macrophage polarization by delivering IL-4, Nano Lett. 17 (5) (2017) 2747–2756.
[21] Y. Li, F. Song, L. Cheng, J. Qian 4, Q. Chen, Functionalized large-pore mesoporous silica microparticles for gefitinib and doxorubicin codelivery, Materials 12 (5) (2019) 766.
[22] Z. Guo, L. Wu, Y. Wang, Y. Zhu, G. Wan, R. Li, Y. Zhang, D. Qian, Y. Wang, X. Zhou, Z. Liu 4, X. Yang, Design of dendritic large-pore mesoporous silica nanoparticles

with controlled structure and formation mechanism in dual-templating strategy, ACS Appl. Mater. Interfaces 12 (16) (2020) 18823–18832.
[23] Z. Li, Y. Zhang, N. Feng, Mesoporous silica nanoparticles: synthesis, classification, drug loading, pharmacokinetics, biocompatibility, and application in drug delivery, Expet Opin. Drug Deliv. 16 (3) (2019) 219–237.
[24] T. Li, S. Shi, S. Goel, X. Shen, X. Xie, Z. Chen, H. Zhang, S. Li, X. Qin, H. Yang, C. Wu 5, Y. Liu, Recent advancements in mesoporous silica nanoparticles towards therapeutic applications for cancer, Acta Biomater. 89 (2019) 1–13.
[25] Y. Zhai, J. Su, W. Ran, P. Zhang, Q. Yin, Z. Zhang, H. Yu, Y. Li, Preparation and application of cell membrane-camouflaged nanoparticles for cancer therapy, Theranostics 7 (10) (2017) 2575–2592.
[26] X. Zhen, P. Cheng, K. Pu, Recent advances in cell membrane-camouflaged nanoparticles for cancer phototherapy, Small 15 (1) (2019), e1804105.
[27] M. Xuan, J. Shao, L. Dai, Q. He, J. Li, Macrophage cell membrane camouflaged mesoporous silica nanocapsules for *in vivo* cancer therapy, Adv. Healthc. Mater. 4 (11) (2015) 1645–1652.
[28] J. Su, H. Sun, Q. Meng, P. Zhang, Q. Yin, Y. Li, Enhanced blood suspensibility and laser-activated tumor-specific drug release of theranostic mesoporous silica nanoparticles by functionalizing with erythrocyte membranes, Theranostics 7 (3) (2017) 523–537.
[29] D. Shao, M. Li, Z. Wang, X. Zheng, Y.H. Lao, Z. Chang, F. Zhang, M. Lu, J. Yue, H. Hu, H. Yan, L. Chen, W.F. Dong 2, K.W. Leong, Bioinspired diselenide-bridged mesoporous silica nanoparticles for dual-responsive protein delivery, Adv. Mater. 28 (2018), e1801198.
[30] D. Dehaini, X. Wei, R.H. Fang, S. Masson, P. Angsantikul, B.T. Luk, Y. Zhang, M. Ying, Y. Jiang, A.V. Kroll, W. Gao, L. Zhang, Erythrocyte-platelet hybrid membrane coating for enhanced nanoparticle functionalization, Adv. Mater. 29 (16) (2017) 1606209.
[31] H.Y. Chen, J. Deng, Y. Wang, C.Q. Wu, X. Li, H.W. Dai, Hybrid cell membrane-coated nanoparticles: a multifunctional biomimetic platform for cancer diagnosis and therapy, Acta Biomater. 112 (2020) 1–13.
[32] M.S. Diamond, D.E. Staunton, S.D. Marlin, T.A. Springer, Binding of the integrin Mac-1 (CD11b/CD18) to the third immunoglobulin-like domain of ICAM-1 (CD54) and its regulation by glycosylation, Cell 65 (1991) 961–971.
[33] R. Palomba, A. Parodi, M. Evangelopoulos, S. Acciardo, C. Corbo, E. de Rosa, I. K. Yazdi, S. Scaria, R. Molinaro, N.E. Toledano Furman, J. You, M. Ferrari, F. Salvatore, E. Tasciotti, Biomimetic carriers mimicking leukocyte plasma membrane to increase tumor vasculature permeability, Sci. Rep. 6 (2016) 34422.
[34] J. Yang, B.C. Furie, B. Furie, The biology of P-selectin glycoprotein ligand-1: its role as a selectin counterreceptor in leukocyte-endothelial and leukocyte-platelet interaction, Thromb. Haemostasis 81 (1) (1999) 1–7.
[35] H. Ye, K. Wang, M. Wang, R. Liu, H. Song, N. Li, Q. Lu, W. Zhang, Y. Du, W. Yang, L. Zhong, Y. Wang, B. Yu, H. Wang, Q. Kan, H. Zhang, Y. Wang, Z. He, J. Sun, Bioinspired nanoplatelets for chemo-photothermal therapy of breast cancer metastasis inhibition, Biomaterials 206 (2019) 1–12.
[36] K. Wang, Y. Zhang, J. Wang, A. Yuan, M. Sun, J. Wu, Y. Hu, Self-assembled IR780-loaded transferrin nanoparticles as an imaging, targeting and PDT/PTT agent for cancer therapy, Sci. Rep. 6 (2016) 27421.
[37] Y. Liu, L. Qiao, S. Zhang, G. Wan, B. Chen, P. Zhou, N. Zhang, Y. Wang, Dual pH-responsive multifunctional nanoparticles for targeted treatment of breast cancer by combining immunotherapy and chemotherapy, Acta Biomater. 66 (2018) 310–324.